nature nanotechnology

ARTICLES

https://doi.org/10.1038/s41565-019-0566-z

An antifouling coating that enables affinity-based electrochemical biosensing in complex biological fluids

Jonathan Sabaté del Río[1,4], Olivier Y. F. Henry[1,5], Pawan Jolly[1] and Donald E. Ingber[1,2,3*]

Affinity-based electrochemical detection in complex biological fluids could enable multiplexed point-of-care diagnostics for home healthcare; however, commercialization of point-of-care devices has been limited by the rapid loss of sensitivity caused by electrode surface inactivation and biofouling. Here, we describe a simple and robust antifouling coating for electrodes consisting of a three-dimensional porous matrix of cross-linked bovine serum albumin supported by a network of conductive nanomaterials composed of either gold nanowires, gold nanoparticles or carbon nanotubes. These nanocomposites prevent non-specific interactions while enhancing electron transfer to the electrode surface, preserving 88% of the original signal after 1 month of exposure to unprocessed human plasma, and functionalization with specific antibodies enables quantification of anti-interleukin 6 in plasma with high sensitivity. The easy preparation, stability and simplicity of this nanocomposite allow the generation of electrochemical biosensors that can operate in complex biological fluids such as blood plasma or serum.

Enzyme-based electrochemical sensors, such as those used in glucometers, have been successfully commercialized and their use is now widespread. However, highly multiplexed enzymatic detection is challenging as the range of enzymes amenable to this method is limited and the optimal activity conditions of each enzyme can vary greatly. Affinity-based electrochemical biosensors (for example, those using antibodies, aptamers and so on) offer a potential alternative for inexpensive, disposable and sensitive multiplexed point-of-care diagnostics for home healthcare. A plethora of assays and surface chemistries in the scientific literature have been successfully implemented using affinity-based electrochemical sensors[1], but commercialization of this technology for clinical diagnostics has been hindered by their inability to maintain sensing functionality when exposed to biological fluids such as plasma or blood[2].

The challenge is that in electrochemical biosensing, the electrode configuration, together with the instrument and sample, conform to a closed electrical and ionic circuit (Fig. 1a) where, unlike in optical biosensors, the interrogation-reading process is coupled. Thus, any materials present in complex samples that bind the electrodes non-specifically will decrease the current and sensitivity. Likewise, traditional antifouling coatings (for example, bovine serum albumin (BSA) and poly(ethylene glycol) self-assembled monolayers (PEG-SAMs))[3] also hinder electron transfer, resulting in a double-edged antifouling strategy[4,5]. Here, we attempted to overcome this problem by creating a three-dimensional (3D) nanocomposite matrix composed of BSA interlaced with conductive nanomaterials including gold nanowires (AuNWs), gold nanoparticles (AuNPs) or carbon nanotubes (CNTs) (Fig. 1b), which sustain electron transfer to the underlying electrode while improving analytical quality parameters[6], and while also reducing non-specific binding and supporting functionalization with antibodies or other bioreceptors. Nanocomposites were prepared by mixing and sonication-centrifugation where homogenization was required, before drop-casting on the surface of gold electrode chips to form a coating (Fig. 1c). Sensor performance was evaluated via cyclic voltammetry, with the electrodes being cycled between oxidation and reduction potentials of an electrochemically active solution of potassium ferri-ferrocyanide (Fig. 1d). Both the peak-to-peak separation (ΔE_p) and current density from this redox process were used to assess electron transfer kinetics between the electrode surface and solution, thus reflecting the overall quality and state of the solid–liquid interface.

While BSA and BSA/AuNW coatings resulted in total passivation, BSA/AuNP and BSA/CNT coatings maintained 25 and 75% of current density (Fig. 1d,e), respectively, in part due to nanoparticle-mediated electron transfer[7–9]. When we measured the antifouling properties of these coatings by carrying out measurements before and after 1-d incubation in buffer containing 1% BSA, all coatings exhibited similarly reduced electrochemical performance except for the BSA/CNTs, which maintained a relatively high current and low ΔE_p, whereas BSA/AuNPs displayed broad ΔE_p up to 0.4 V indicating limited diffusion of ferri-/ferrocyanide to the electrode surface due to biofouling[10,11] (Fig. 1e). To circumvent this limitation, we added glutaraldehyde (GA) to cross-link BSA molecules, thereby creating a porous 3D protein matrix impregnated with conducting nanomaterials (Fig. 1b) and thus improving overall electrochemical performance. However, total passivation of the BSA/AuNP/GA composite occurred due to plugging of matrix pores by nanoparticles (Fig. 1d,e). After 1-d incubation in 1% BSA, the BSA/AuNW/GA coating maintained 92% of current density and $\Delta E_p = 110$ mV. To assess the mass transport of potassium ferri-/ferrocyanide on BSA/AuNW/GA-coated electrodes, we evaluated voltammograms at different scan rates, which generated profiles similar to those observed on bare gold electrodes (Fig. 1f) and currents proportional to the square root of the scan rate, indicating a diffusion-limited process (Fig. 1g).

[1]Wyss Institute for Biologically Inspired Engineering at Harvard University, Boston, MA, USA. [2]Harvard John A. Paulson School of Engineering and Applied Sciences, Harvard University, Cambridge, MA, USA. [3]Vascular Biology Program and Department of Surgery, Boston Children's Hospital and Harvard Medical School, Boston, MA, USA. [4]Present address: Center for Soft and Living Matter, Institute for Basic Science, Ulsan, Republic of Korea. [5]Present address: Imec, Leuven, Belgium. *e-mail: don.ingber@wyss.harvard.edu

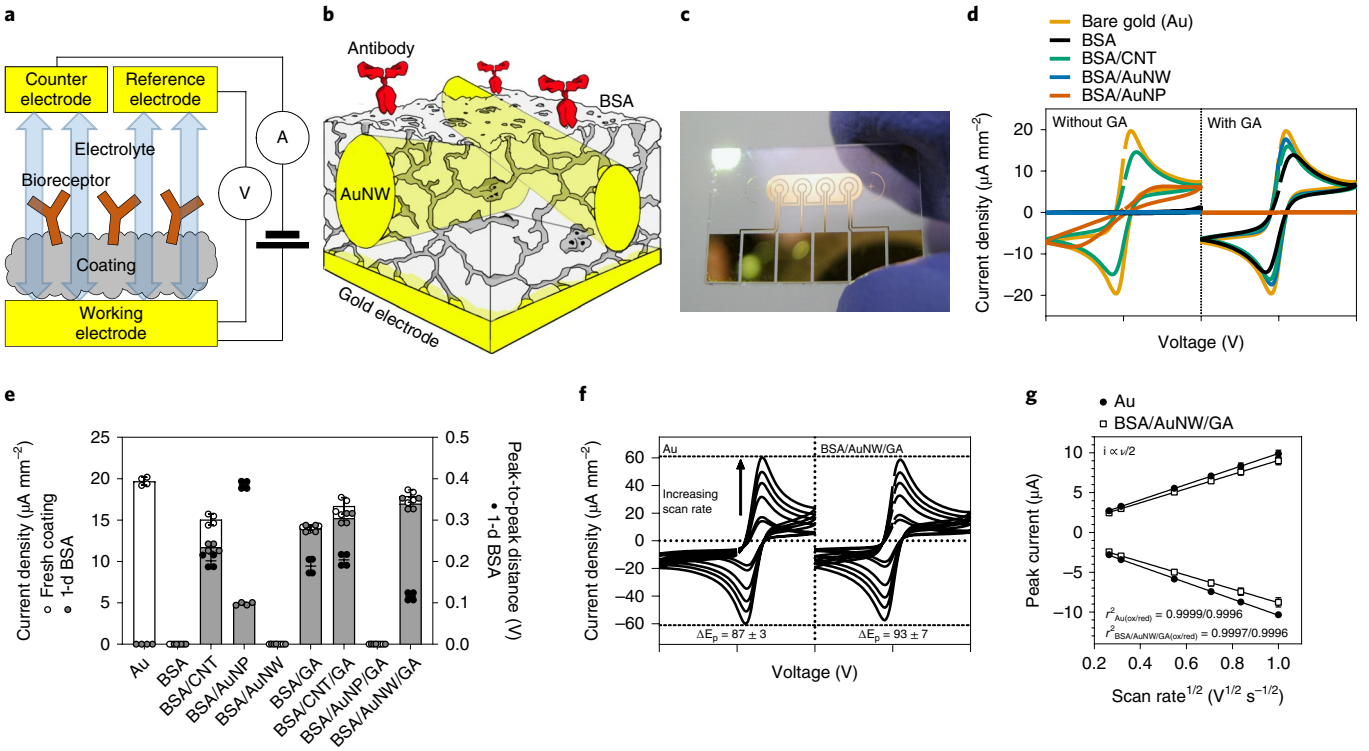

Fig. 1 | The nanocomposite coating. a, Schematic of the three-electrode electrochemical set-up used. **b**, Schematic of the BSA/AuNW/GA coating functionalized with antibodies on a gold electrode. **c**, Photograph of an electrode chip consisting of four working electrodes with a common reference and counter-electrode. **d**, Typical voltammograms showing oxidation and reduction peaks of an equimolar solution of 5 mM ferri-/ferrocyanide of various nanocomposite-coated electrodes (left) and 1% GA-cross-linked nanocomposite-coated electrodes (right). **e**, Electrochemical characterization of various electrode coatings. Bars are the mean values of the current densities of various nanocomposite-coated electrodes before (white) and after (grey) 1-d exposure to 1% BSA; black circles denote the final mean value of peak-to-peak distances ($n = 4$ independent electrodes). **f**, Voltammograms of bare gold- (left) and BSA/AuNW/GA-coated electrodes (right) of an equimolar solution of 5 mM ferri-/ferrocyanide at different scan rates (0.07–1.0 V s^{-1}). **g**, Extracted oxidation/reduction peak current (i_p) mean values (circles) from the voltammograms shown in **f** plotted versus the square root of the scan rate ($n = 4$ independent electrodes). Error bars in all graphs represent the s.d. of the mean.

To better understand these enhanced electrochemical properties, we characterized the porosity and topography of the coating using transmission electron microscopy (TEM), which revealed that, during nanocomposite formation, BSA proteins adsorb around the wires through hydrophobic and electrostatic interactions with cetrimonium bromide, a positively charged ionic surfactant used to stabilize AuNWs[12] (Supplementary Fig. 1). After BSA is cross-linked with GA, a thicker, porous, sponge-like protein matrix is generated (Supplementary Fig. 1). This was confirmed by scanning electron microscopy (SEM) analysis (Fig. 2a), revealing aggregates on BSA/GA-coated electrodes (Fig. 2a) similar to those observed in BSA nanoparticles used for drug delivery[13–15]. The most extensive porosity was observed in BSA/AuNW/GA coatings occupying 7.5 ± 0.5% of the total area, with an average pore density of 71 ± 9 pores μm^{-2}, average pore radius of 29 ± 3 nm and average nearest-neighbour distance between pores of 59.9 nm. Atomic force microscopic (AFM) analysis confirmed that addition of AuNWs to the GA-cross-linked BSA composite increased the roughness of the coating due to pore formation (Fig. 2b and Supplementary Fig. 2), with an average pore depth of 4.3 ± 1.0 nm (Fig. 2c) and maximum pore depth of 7.9 ± 0.6 nm.

Electrochemical behaviour

Considering the porosity of the BSA/AuNW/GA-coated electrodes and their excellent electrochemical properties, we hypothesized that the coating behaves as a recessed nanoelectrode ensemble with each pore acting as an individual nanoelectrode. Similar behaviour has been observed in thermoresponsive hydrogel-coated electrodes displaying different steady-state or transient voltammogram responses depending on the shrunken or swollen state of the hydrogel, resulting from through-film transport or pore diffusion of electroactive species[16]. The electrochemical behaviour of a nanoelectrode ensemble depends on the size of each nanoelectrode, the recesses, the pore-to-pore distance, the diffusion coefficient of the species in solution and the time scale of the experiment, which is determined in cyclic voltammetry by the scan rate[17]. At fast scan rates the diffusion through each pore is independent and the overall ensemble displays a planar diffusion profile, whereas at slower scan rates the diffusion layers outgrow the pores and display a semi-infinite radial diffusion profile with sigmoidal voltammogram responses—that is, a sigmoidal-shaped voltammogram with all nanoelectrodes contributing to the overall current. At very slow scan rates, or in the case where the pore-to-pore distance is not sufficiently large, the diffusion layer of each AuNW or pore will overlap with adjacent diffusion layers to yield a semi-infinite linear diffusion profile with typical transient voltammograms and overall currents similar to those observed in a macro-electrode[18,19]. We observed that, for a range of scan rates, the BSA/AuNW/GA-coated electrodes display transient voltammograms (Fig. 1f) suggesting overlapped diffusion profiles due to the short pore-to-pore distances. A simple model considering only the diffusion of the electro-active species and pore-to-pore distances, and the model of Guo and Lindner[17] (which also takes

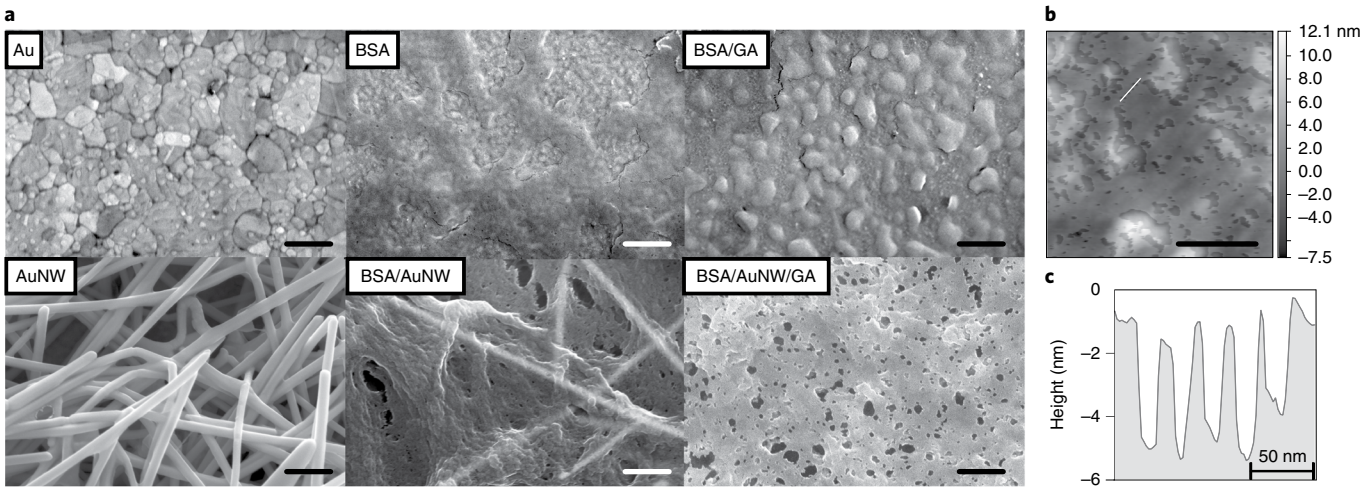

Fig. 2 | Characterization of the BSA/AuNW/GA nanocomposite. a, Scanning electron micrograph of the coated electrodes (scale bar, 400 nm). This analysis was repeated twice on different samples. **b**, AFM topography of BSA/AuNW/GA-coated mica. **c**, Height profile extracted from the white line in **b**.

into account pore size, recess and scan rate), predict overlapping of diffusion profiles between the pores because the distance between the pores is shorter than the distance diffused by the electro-active species (see Methods).

Although we observed some current in the BSA/AuNP-coated electrodes, the cross-linking in BSA/AuNP/GA passivated the electrode (Fig. 1d, left versus right). To understand this behaviour, we carried out a further study based on the hypothesis that the BSA layer formed on the electrodes at this concentration is insulating, as seen for BSA-coated electrodes (Fig. 1d), but that charge transfer between electro-active species in solution and the electrodes can happen at the surface of AuNPs through nanoparticle-mediated electron transfer when these particles are uncovered and located at the distal end of a thin organic coating[8,9], as we observed here (Supplementary Figs. 3 and 4a). TEM and SEM images of the BSA/AuNP coating revealed that, unlike the case of AuNWs, BSA adsorption on AuNPs is limited due to electrostatic repulsion between BSA and the well-dispersed, citrate-capped AuNPs[20] (Supplementary Figs. 1 and 3). AFM measurements showed that, because BSA coating thickness is relatively thin (Supplementary Fig. 4b), by controlling particle-to-particle distance and scan rate we achieved different diffusion regimes with either quasi-steady-state or transient voltammograms (Supplementary Fig. 4c). SEM images revealed nanoparticle concentrations of 6.7 μm^{-2} (Supplementary Fig. 3) corresponding to an average particle-to-particle distance of 193 nm, which is sufficiently disperse to ensure quasi-steady-state electrochemical behaviour[17].

Moreover, the impedance for the BSA/AuNP-coated electrodes shows semi-circular profiles (Supplementary Fig. 4d), like those previously observed for ultra-low-density, randomly grown, vertically aligned carbon nanofibres due to nanoelectrode size[21]. Unlike AuNWs, the AuNPs do not merge within the BSA matrix during cross-linking and thus they finally clog the pores because their diameter (20 nm) is >89% that of the pores in the coating (Supplementary Fig. 4e). As a result of this clogging, different pore morphology and density can be observed when comparing the SEM micrographs for BSA/AuNW/GA versus BSA/AuNP/GA, with the latter clearly showing smaller and fewer pores (Supplementary Fig. 3). As the thickness of the cross-linked nanocomposite increases (Supplementary Fig. 4f), the electron transfer kinetics becomes hindered and charge transfer from electro-active species in solution to the underlying electrode is not possible because of limited diffusion and, as previously shown, the presence of even a very thin organic coating on top of nanoparticles (Fig. 1d) passivates the electrodes[7].

Antifouling mechanism

The antifouling properties of the BSA/AuNW/GA coatings also arise from the enhanced porosity of the cross-linked BSA matrix, which efficiently size-excludes particles that are too large to diffuse through the pores, thereby blocking their access to the electrode surface[22]. In our case, 69% of the pores present on the surface of the coating are smaller in diameter than the typical effective length of 18.1 nm for a BSA protein under physiological conditions[23]. BSA has an isoelectric point of ~4.7 at which it tends to aggregate, but aggregation is prevented at physiological pH. In this manner, non-specific adsorption of soluble albumin molecules present in the assay (albumin accounts for ~60% of total protein in plasma) is prevented due to charge repulsion, and so we used this abundant protein, which is normally a major cause of fouling, to our advantage.

To explore this further, we carried out a control study to determine whether a small and positively charged protein in plasma could potentially adsorb onto the coating through electrostatic attraction and clog the pores. Human prostate-specific antigen (PSA), a 34-kD glycoprotein with a positive electrostatic surface potential and a net charge of +5 (ref. [24]), was incubated on BSA/AuNW/GA-coated electrodes that were either unfunctionalized or functionalized using carbodiimide conjugation chemistry with an anti-IL-6 antibody or an anti-PSA antibody. When we carried out an electrochemical enzymatic sandwich detection assay with horseradish peroxidase (HRP)-labelled anti-PSA antibody, we observed a redox current for the positive control but no signal for the unfunctionalized BSA/AuNW/GA-coated electrode, nor with that functionalized with anti-IL-6 antibody (Supplementary Fig. 5a,b). Thus, electrostatic interactions between positively charged proteins and BSA from the coating are not sufficiently strong to sustain fouling or clogging of the pores.

Cross-linking mechanism

BSA cross-linked with GA has previously been reported to produce 3D nanostructures in the form of porous hydrogels[25]. During protein cross-linking, several functional groups can react with GA, including amines, thiols, phenols and imidazoles. When we analysed the location of potential reactive groups in lysine, tyrosine, tryptophan, histidine, cysteine and arginine residues within the BSA protein (PDB ID: 4F5S) we found that, unlike other residues, most of the ε-amines from lysine residues are exposed on the solvent-accessible surface (Van der Waals distance = +1.5 Å) of the protein (Fig. 3a), which is in agreement with previous findings indicating that cross-linking between proteins and GA occurs predominantly through lysine residues[26].

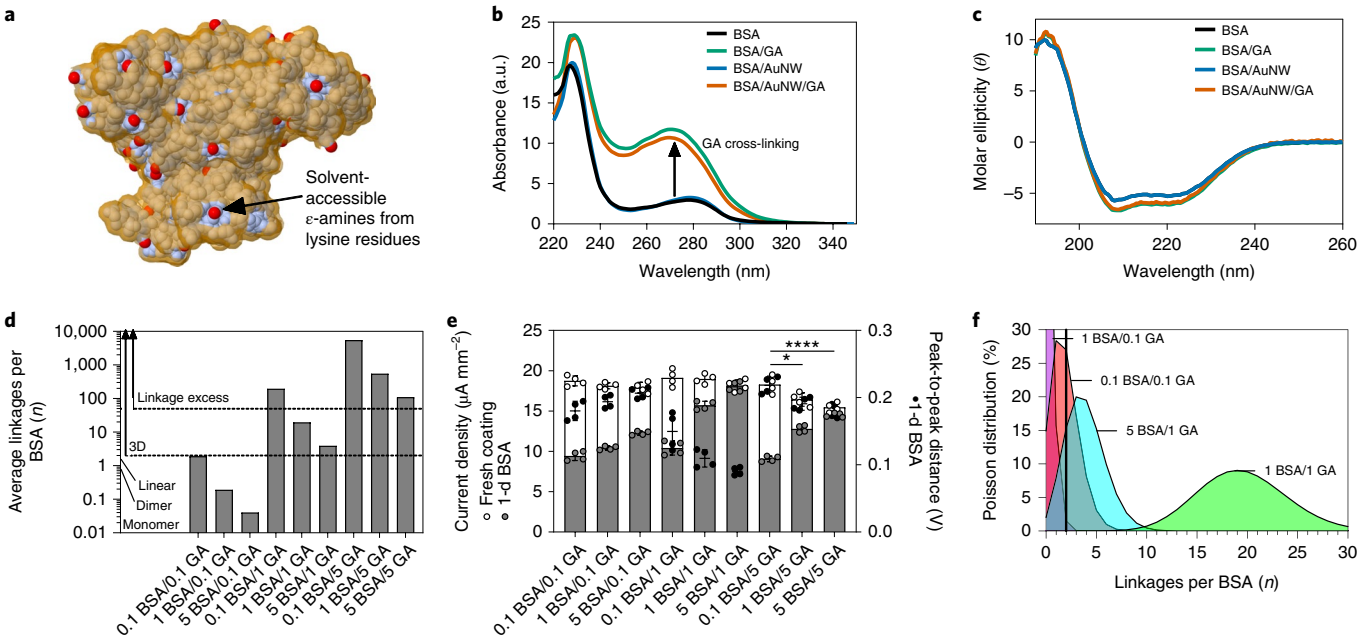

Fig. 3 | Cross-linking of BSA with GA. a, Solid representation of a BSA protein (PDB ID: 4F5S) highlighting the ε-amine groups from lysine residues (red) within the solvent-accessible layer. **b**, UV absorption and **c**, circular dichroism spectra of BSA when mixed with/without GA and/or AuNW. a.u., arbitrary units. **d**, Average linkage per BSA calculated for different coatings where BSA ranges from 0.1 to 5 mg ml^{-1} and GA from 0.1 to 5%. The parallel broken lines between 2 and 50 define the useful range where we can expect to find a 3D BSA matrix without excess GA. **e**, Optimization and characterization of the BSA/AuNW/GA coating with different BSA/GA formulations ($n = 4$ independent electrodes). White bars represent the mean value of current density for a fresh coating, grey bars represent 1-d incubation in 1% BSA and black circles represent the mean value of the peak-to-peak separation after 1-d incubation in 1% BSA; error bars represent s.d. of the mean. The statistical analysis is a two-way ANOVA (two-sided, $\alpha = 0.05$) for current density and peak-to-peak separation of fresh coatings with Tukey's multiple comparisons test; $^{*}P < 0.05$, $^{**}P < 0.01$, $^{***}P < 0.001$, $^{****}P < 0.0001$. **f**, Poisson distribution showing discrete linkage probability distribution for BSA molecules in different coatings.

Although the cross-linking reaction is not clearly understood, a simple mechanism involving Schiff base with both ends of monomeric GA has long been ruled out since the reversibility of this reaction contradicts the irreversible cross-linking conjugation observed experimentally[26,27]. In the presence of primary amines, GA can react quickly to yield polymers of pyridine, which are the structural glue responsible for cross-linking[27]. The products of this rapid cross-linking mechanism are 3D molecular networks, and the reaction can be followed as an increase in absorbance at 265–270 nm (ref. [27]; Fig. 3b and Supplementary Fig. 6a) while the native conformation of the protein is maintained as observed by circular dichroism spectroscopy (Fig. 3c and Supplementary Fig. 6b). Although the reaction yielding large products occurs within minutes, consolidation of larger structures occurs with the ageing[18] and accessibility of lysine residues[26], as we corroborated with a 24-h incubation experiment (Supplementary Fig. 7a). This is consistent with previous work showing that incubation times of 18 h or more are required to form BSA nanoparticles through cross-linking with GA[13–15].

The pyridine polymer formation mechanism requires at least five GA molecules to yield an effective polymer cross-linking between two amines, effectively forming a linkage between two BSA proteins; thus, the average number of linkages per BSA can be used to predict the morphology of the final product[27]. Composites with two, one or fewer linkages per BSA will yield linear BSA polymers, dimers or monomers, respectively, whereas those with an average number of linkages similar to, or higher than, the number of available reactive amino acids (54) will yield highly cross-linked and compact BSA polymers with an excess of unreacted GA on their surface. The excess of pyridine polymers on the surface of these coatings will probably react with fouling proteins, blocking and clogging the pores, and thus result in poor antifouling capacity.

Quantification of the average number of linkages per BSA for the coatings formulated as 0.1 BSA/0.1 GA, 1 BSA/0.1 GA and 5 BSA/0.1 GA revealed that the BSA polymers yield mostly dimers and monomers (Fig. 3d), whereas the 0.1 BSA/1 GA, 0.1 BSA/5 GA, 1 BSA/5 GA and 5 BSA/5 GA coatings are heavily cross-linked (Fig. 3d). The 1 BSA/1 GA and 5 BSA/1 GA coatings have an average of 22 and four linkages between BSA particles, respectively and, in this case, a 3D matrix forms (Fig. 3d), which is in agreement with these two coatings exhibiting the best antifouling performance (Fig. 3e).

Moreover, we expect that a 3D coating with good performance should also be homogeneously cross-linked with well-defined pore sizes and number of linkages per BSA. If the number of linkages per BSA protein is a discrete probability distribution (see Methods), the composite 5 BSA/1 GA will have a narrower distribution of bonds per BSA molecule (Fig. 3f), with 80% of the BSA protein molecules bound to between one and six other BSA proteins. In contrast, the 1 BSA/1 GA coating has a higher average number of linkages per BSA and a broader distribution (80% of BSA proteins have 16–28 linkages), thus leading to more heterogeneous and compact coatings with smaller pore size. This explains why the current density for the 1 BSA/1 GA coating is slightly lower with a broader peak-to-peak separation (Fig. 3e). All in all, the optimal BSA/AuNW/GA contained 5 mg ml^{-1} BSA, 1% GA and ≥50 μg ml^{-1} AuNW considering highest current density, smallest peak-to-peak distance and lowest drop in performance after 1-d incubation in 1% BSA.

Analysis in plasma

For clinical diagnostics, it is crucial to understand the performance of sensors in complex biological fluids. We therefore challenged the electrochemical sensors coated with the optimized BSA/AuNW/GA nanocomposite by incubating them in either

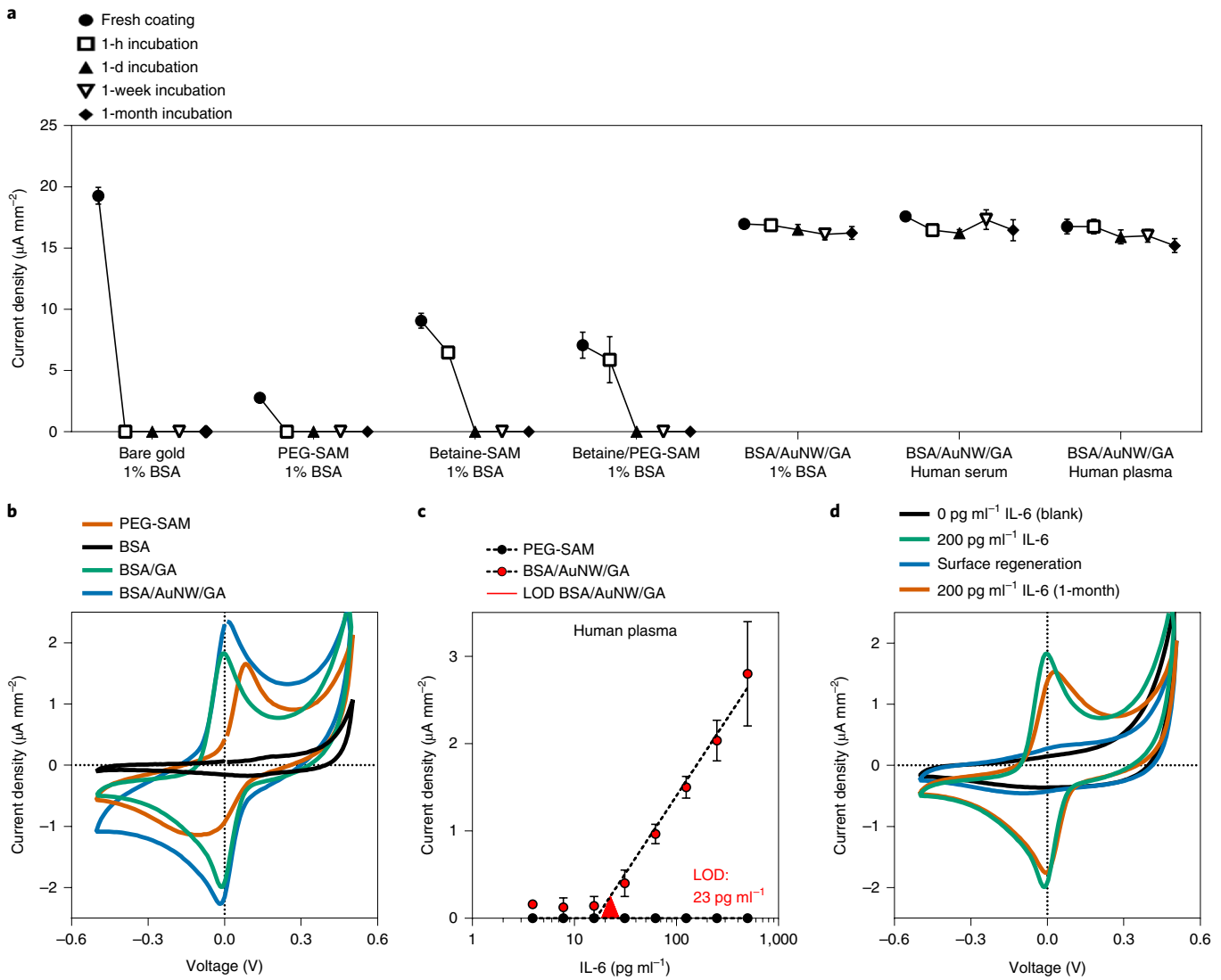

Fig. 4 | Coating antifouling properties and biosensing performance. a, Comparison of mean value of current densities recorded at bare gold electrodes, PEG-SAM-modified electrodes, betaine-SAM-, betaine/PEG-SAM- and optimized BSA/AuNW/GA-coated electrodes stored for >30 d at 4 °C in 1% BSA, human serum or human plasma ($n = 4$ independent electrodes, error bars represent the s.d. of the mean). **b**, Comparison of TMB oxidation and reduction peaks on IL-6 biosensor (assay carried out in PBS) fabricated using BSA/GA, PEG-SAM and BSA/AuNW/GA. **c**, Calibration curve for the detection of IL-6 in unprocessed human plasma for BSA/AuNW/GA-coated electrodes (red) and electrodes prepared using a PEG-SAM-based surface chemistry (black). $n = 4$ independent electrodes, circles represent the mean value of current density and error bars represent the s.d. of the mean. **d**, Cyclic voltammograms recorded following the completion of the IL-6 assay on a fresh BSA/AuNW/GA-coated electrode, and the regeneration of capture antibodies in glycine and assay repetition after 1 month.

1% BSA, unprocessed human serum or plasma. Impressively, the BSA/AuNW/GA coating demonstrated excellent antifouling behaviour in these fluids with only minimal (~7%) loss of sensitivity after 1-month exposure (Fig. 4a). The same scenario using PEG-SAM-coated gold electrodes resulted in total passivation after 1-h incubation (Fig. 4a) as expected[28], whereas betaine-SAM and betaine/PEG-SAM withheld up to 80% of the current density after 1-h incubation in 1% BSA, but the current densities recorded immediately after formation of these coatings were at least 50% lower than those observed for bare gold (Fig. 4a). In contrast, the current densities displayed by the BSA/AuNW/GA nanocomposite coating remained high and were comparable to those of the native gold electrode even after 1-month exposure to complex fluids (Fig. 4a).

This approach was adapted to develop an affinity-based electrochemical sensor by functionalizing the BSA/AuNW/GA coating with an antibody directed against clinically relevant target biomolecules, including the inflammatory cytokine Interleukin-6 (IL-6), insulin and glucagon hormones. An electrochemical enzymatic sandwich detection assay was carried out, by sequentially incubating the electrodes coated with target-specific antibodies with soluble IL-6, insulin or glucagon, biotinylated anti-target detection antibodies, streptavidin conjugated to HRP and finally the addition of a formulation of tetramethylbenzidine (TMB) that precipitates on the surface coating of the electrode when oxidized by HRP, yielding an electro-active product that can be detected using cyclic voltammetry[29]. The voltammogram revealed irreversible electrochemical oxidation in the case of PEG-SAM-coated electrodes, whereas well-defined redox peaks were obtained for BSA/AuNW/GA-coated electrodes (Fig. 4b). These studies confirmed that IL-6, insulin and glucagon could readily be detected using BSA/AuNW/GA-coated electrochemical sensors in both PBS (Supplementary Fig. 8a) and

1% BSA (Supplementary Fig. 8b–d). More importantly, IL-6 could be detected in unprocessed human plasma with a limit of detection (LOD) of 23 pg ml^{-1} (Fig. 4c) but, in contrast, electrode chips prepared with anti-IL-6 antibodies immobilized on a PEG-SAM base could be detected only in PBS (Supplementary Fig. 8a) and no signal was detected at all in complex fluids such as plasma (Fig. 4c). Additionally, fabrication of the chip and detection of IL-6 in human plasma could be followed step-by-step by measuring the difference in charge transfer resistance (R_{ct}) of the biosensor by electrochemical impedance spectroscopy (EIS) (Supplementary Fig. 9).

Although BSA/AuNW/GA-coated electrodes stored in 1% BSA at 4 °C maintained good current (Supplementary Fig. 7b), the shelf-life of a biosensor may be limited by the stability of the functionalized bioreceptor due to degradation or detachment caused by surface regeneration. When we functionalized the BSA/AuNW/GA-coated electrodes with anti-IL-6 antibodies, we were successful in regenerating and repeating electrochemical sensing assays by washing used electrode chips with 2 mM glycine hydrochloride (Fig. 4d). This allowed us to detect 200 pg ml^{-1} IL-6, regenerate the surface to repeat the assay and repeat the process after storage for 1 week and 1 month in 1% BSA (Fig. 4d), with minimum 1 current density loss (Supplementary Fig. 7c).

Conclusion

In summary, we have demonstrated that a simple drop-casting method can be used to coat electrodes with a 3D porous BSA matrix impregnated with highly conductive nanomaterials that are collectively cross-linked with GA. This provides enhanced antifouling properties while retaining electrochemical performance even after long-term exposure to complex biological fluids. The porous BSA backbone of the matrix prevents non-specific protein adsorption, while allowing diffusion of soluble electro-active species through to the electrode with minimal hindrance as compared to traditional antifouling coatings. Fabrication conditions were optimized to achieve optimal porosity and stability, and to avoid undesired cross-linker reactivity. As a result, the gold electrodes retained >88% current density after coating with the BSA/AuNW/GA nanocomposite and there was a signal loss of only ~10% after 1-month storage in direct contact with unprocessed human plasma at 4 °C, showing a significantly better performance than other state-of-the-art antifouling coatings (Supplementary Table 1). We also demonstrated the potential commercial and clinical utility of this approach with a highly specific biosensor for the detection of inflammatory cytokine IL-6 in unprocessed human plasma, as well as two hormones (insulin and glucagon) in 1% BSA. Moreover, these biosensors can be reused after washing with minimal signal loss, allowing repeated measurements when continuous monitoring of biomarkers is required. This method can be extended to other substrates and bioreceptors where sensitive detection in a complex matrix is required, and thus they may be useful in the development of both enzyme- and affinity-based electrochemical sensors in various medical and non-medical applications, including in-hospital biodetection, environmental toxin sensing, small-molecule detection and implantable medical devices, as well as for point-of-care diagnostics.

Data availability

The data that support the plots within this paper and other findings of this study are available from the authors upon reasonable request.

Reporting Summary. Further information on research design is available in the Nature Research Reporting Summary linked to this article.

Online content

Any methods, additional references, Nature Research reporting summaries, source data, extended data, supplementary information, acknowledgements, peer review information, details of author contributions and competing interests, and statements of code and data availability are available at https://doi.org/10.1038/s41565-019-0566-z.

Received: 5 March 2019; Accepted: 1 October 2019;
Published online: 11 November 2019

References

1. Dugas, V., Elaissari, A. & Chevalier, Y. in *Recognition Receptors in Biosensors* (ed Zourob, M.) 47–134 (Springer, 2010).
2. Barfidokht, A. & Gooding, J. J. Approaches toward allowing electroanalytical devices to be used in biological fluids. *Electroanalysis* **26**, 1182–1196 (2014).
3. Campuzano, S., Pedrero, M., Yáñez-Sedeño, P. & Pingarrón, J. M. Antifouling (bio)materials for electrochemical (bio)sensing. *Int. J. Mol. Sci.* **20**, 423 (2019).
4. Chen, S., Li, L., Zhao, C. & Zheng, J. Surface hydration: principles and applications toward low-fouling/nonfouling biomaterials. *Polymers* **51**, 5283–5293 (2010).
5. Banerjee, I., Pangule, R. C. & Kane, R. S. Antifouling coatings: recent developments in the design of surfaces that prevent fouling by proteins, bacteria, and marine organisms. *Adv. Mater.* **23**, 690–718 (2011).
6. Kumar, S., Ahlawat, W., Kumar, R. & Dilbaghi, N. Graphene, carbon nanotubes, zinc oxide and gold as elite nanomaterials for fabrication of biosensors for healthcare. *Biosens. Bioelectron.* **70**, 498–503 (2015).
7. Shein, J. B., Lai, L. M. H., Eggers, P. K., Paddon-Row, M. N. & Gooding, J. J. Formation of efficient electron transfer pathways by adsorbing gold nanoparticles to self-assembled monolayer modified electrodes. *Langmuir* **25**, 11121–11128 (2009).
8. Gooding, J. J., Alam, M. T., Barfidokht, A. & Carter, L. Nanoparticle mediated electron transfer across organic layers: from current understanding to applications. *J. Braz. Chem. Soc.* **25**, 418–426 (2014).
9. Barfidokht, A., Ciampi, S., Luais, E., Darwish, N. & Gooding, J. J. Distance-dependent electron transfer at passivated electrodes decorated by gold nanoparticles. *Anal. Chem.* **85**, 1073–1080 (2013).
10. Bard, A. & Faulkner, L. *Electrochemical Methods: Fundamentals and Applications* (John Wiley & Sons, Inc., 2001).
11. Elgrishi, N. et al. A practical beginner's guide to cyclic voltammetry. *J. Chem. Educ.* **95**, 197–206 (2018).
12. Alam, S. & Mukhopadhyay, A. Conjugation of gold nanorods with bovine serum albumin protein. *J. Phys. Chem. C* **118**, 27459–27464 (2014).
13. Sripriyalakshmi, S., Anjali, C. H., George, P. D., Rajith, B. & Ravindran, A. BSA nanoparticle loaded atorvastatin calcium—a new facet for an old drug. *PLoS ONE* **9**, e86317 (2014).
14. Bronze-Uhle, E. S., Costa, B. C., Ximenes, V. F. & Lisboa-Filho, P. N. Synthetic nanoparticles of bovine serum albumin with entrapped salicylic acid. *Nanotechnol. Sci. Appl.* **10**, 11–21 (2017).
15. Yu, Z., Yu, M., Zhang, Z., Hong, G. & Xiong, Q. Bovine serum albumin nanoparticles as controlled release carrier for local drug delivery to the inner ear. *Nanoscale Res. Lett.* **9**, 343–343 (2014).
16. Kaniewska, K., Kyriacou, K., Donten, M., Stojek, Z. & Karbarz, M. Micro- and nanoelectrode array behavior at regularly sized electrode modified with a thin film of thermoresponsive polymeric gel. *Electrochim. Acta* **290**, 595–604 (2018).
17. Guo, J. & Lindner, E. Cyclic voltammograms at coplanar and shallow recessed microdisk electrode arrays: guidelines for design and experiment. *Anal. Chem.* **81**, 130–138 (2008).
18. Ordeig, O., del Campo, J., Muñoz, F. X., Banks, C. E. & Compton, R. G. Electroanalysis utilizing amperometric microdisk electrode arrays. *Electroanalysis* **19**, 1973–1986 (2007).
19. Moretto, L. M. & Kalcher, K. *Environmental Analysis by Electrochemical Sensors and Biosensors* (Springer, 2014).
20. Brewer, S. H., Glomm, W. R., Johnson, M. C., Knag, M. K. & Franzen, S. Probing BSA binding to citrate-coated gold nanoparticles and surfaces. *Langmuir* **21**, 9303–9307 (2005).
21. Siddiqui, S., Arumugam, P. U., Chen, H., Li, J. & Meyyappan, M. Characterization of carbon nanofiber electrode arrays using electrochemical impedance spectroscopy: effect of scaling down electrode size. *ACS Nano* **4**, 955–961 (2010).
22. Patel, J. et al. Electrochemical properties of nanostructured porous gold electrodes in biofouling solutions. *Anal. Chem.* **85**, 11610–11618 (2013).
23. Jachimska, B., Tokarczyk, K., Łapczyńska, M., Puciul-Malinowska, A. & Zapotoczny, S. Structure of bovine serum albumin adsorbed on silica investigated by quartz crystal microbalance. *Colloids Surf. A* **489**, 163–172 (2016).

24. Villoutreix, B. O., Griffin, J. H. & Getzoff, E. D. A structural model for the prostate disease marker, human prostate-specific antigen. *Protein Sci.* **3**, 2033–2044 (1994).
25. Ma, X. et al. A biocompatible and biodegradable protein hydrogel with green and red autofluorescence: preparation, characterization and in vivo biodegradation tracking and modeling. *Sci. Rep.* **6**, 19370 (2016).
26. Migneault, I., Dartiguenave, C., Bertrand, M. J. & Waldron, K. C. Glutaraldehyde: behavior in aqueous solution, reaction with proteins, and application to enzyme crosslinking. *Biotechniques* **37**, 790–802 (2004).
27. Johnson, T. J. A. in *Biocatalyst Design for Stability and Specificity*, Vol. 516 (eds Himmel, M. E. & Georgiou, G.) 283–295 (American Chemical Society, 1993).
28. Phan, H. T. M., Bartelt-Hunt, S., Rodenhausen, K. B., Schubert, M. & Bartz, J. C. Investigation of bovine serum albumin (BSA) attachment onto self-assembled monolayers (SAMs) using combinatorial quartz crystal microbalance with dissipation (QCM-D) and spectroscopic ellipsometry (SE). *PLoS ONE* **10**, e0141282 (2015).
29. Fanjul-Bolado, P., González-García, M. B., Costa-García, A. J. A. & Chemistry, B. Amperometric detection in TMB/HRP-based assays. *Anal. Bioanal. Chem.* **382**, 297–302 (2005).

Methods

Nanocomposite preparation. The BSA/AuMW nanocomposite was prepared by mixing 1 ml AuNW dispersion at ≥50 μg ml^{-1} (diameter 30 nm, length 4,500 nm; Sigma-Aldrich, no. 716944) with 5.0 mg BSA (Sigma-Aldrich, product no. A7906) and sonication for 5 min (Bransonic, CPX 3800). The BSA/AuNP composite was prepared by mixing 1 ml AuNP (diameter 20 nm; Sigma-Aldrich, no. 741965) dispersion (~6.54×10^{11} particles ml^{-1}) with 5.0 mg BSA. The BSA/CNT composite was prepared by mixing 1.0 mg CNT (diameter 1.1 nm, length 5–30 μm; US Research Nanomaterials, Inc., no. US4112) and 5.0 mg BSA in 1 ml PBS. The mixture was sonicated in a tip sonicator for 30 min with on/off intervals of 1 s at 50% amplitude, 125 W and 20 kHz (Qsonica Q125), yielding an opaque black solution with a foam layer. After centrifugation at 16.1 relative centrifugal force for 15 min, the semi-transparent solution was recovered and the black precipitate discarded. Composites were stored at 4 °C.

Electrode coating and functionalization. The electrode chips were sonicated with isopropyl alcohol for 5 min to remove the protective resin, and the surface was cleaned with oxygen plasma (2 min, 0.5 mbar O_2, 50 W). A coating solution consisting of 69 μl of nanocomposite solution (containing either CNT, AuNP, 1:1,000 dilution of AuNP, AuNW or only BSA as a control) was directly mixed with 1 μl of 70% GA (Sigma-Aldrich, no. G7776) by pipetting, rapid drop-casting on each electrode chip and maintenance in a water-saturated atmosphere for 24 h at room temperature. The electrode chips were rinsed with PBS (Thermo Fisher Scientific, no. 14190144) in a shaker for 30 min. At this point the electrode chips can either be functionalized using carbodiimide chemistry or stored in a N_2 atmosphere at 4 °C for 5 weeks. For comparative studies, further electrode chips were coated with a self-assembled monolayer of either a carboxylic bipodal PEGylated alkanethiol (22-(3,5-bis((6-mercaptohexyl) oxy)phenyl)-3,6,9,12,15,18,21-heptaoxadocosanoic acid dithiol) (PEG-SAM; SensoPath Technologies, no. SPT-0014A6), a sulfobetaine3-undecanethiol (*N*-(11-mercaptoundecyl)-*N*,*N*-dimethyl-3-ammonio-1-propanesulfonate) (betaine-SAM; Dojindo Molecular Technologies Inc., no. S350-10) or a 10:1 co-immobilization of sulfobetaine3-undecanethiol with thiol-PEG4-acid (1-mercapto-3,6,9,12-tetraoxapentadecan-15-oic acid)-labelled betaine/PEG-SAM (Broadpharm, no. BP-21116). To prepare the PEG-SAM electrodes, 10 μl of an ethanolic solution of 1 mM of carboxylic bipodal PEGylated alkanethiol was drop-cast on a clean electrode chip and allowed to form a SAM for 24 h in an ethanol-saturated atmosphere, after which the electrodes were rinsed in ethanol. In the case of betaine-SAM and betaine/PEG-SAM, 10 μl of PBS solution of sulfobetaine3-undecanethiol 20 μM or co-immobilization of 200 μM sulfobetaine3-undecanethiol and 20 μM thiol-PEG4-acid, respectively, was drop-cast and allowed to form a SAM for 24 h in a water-saturated atmosphere, after which the electrodes were thoroughly rinsed in PBS. At this point the electrode chips can be either functionalized—for instance, with carbodiimide chemistry—or stored in a N_2 atmosphere for up to 1 week to prevent oxidation of the thiol groups. The carboxylic end of PEG-SAM was neutralized with ethanolamine (Sigma-Aldrich, no. E9508) before any fouling study.

Redox species can undergo electron transfer with AuNP[7] or CNTs[7] when immobilized at the distal end of an electrode coated with a passivating organic layer, rather than tunnelling across the insulating layer[8]. For very thin coatings (<20 Å), the electron transfer kinetics is independent of thickness and voltammograms such as those of pristine electrodes are observed. As the thickness of the layer increases (>20 Å), as in the present study, electron transfer kinetics are hindered and the electrodes gradually passivate[9]. Additionally, the sonication of BSA/CNT drives an irreversible change in BSA structure, different from thermal denaturation, which enhances surface activity, hydrophobicity and charge leading to non-covalent protein aggregate[30]. BSA proteins also interact non-covalently with CNT through hydrophobic and van der Waals interactions, forming protein coronas that increase their solubility[31,32]; therefore, a large portion of BSA was discarded after centrifugation. By measuring the ultraviolet (UV) absorption of the BSA/CNT solution at 280 nm after sonication and centrifugation (Supplementary Fig. 1a), we were able to estimate the concentration of BSA; however, the interaction between BSA and carboxylated CNT can generate hyperchromicity, enhancing UV absorption at 280 nm due to altered conformation of the aromatic amino acid residues binding to the CNT[33]. This effect is more evident in the BSA/CNT/GA (Supplementary Fig. 1a), and could lead to an overestimation of free BSA protein in BSA/CNT and, therefore, the BSA concentration was no higher than 3.6 mg ml^{-1} (versus 4.89 ± 0.12 mg ml^{-1} in other nanocomposite formulations).

Electrochemical characterization of electrodes and coatings. All electrochemical experiments were carried out on planar microfabricated chips (Supplementary Information) containing four working electrodes (geometric area 0.159 mm^2 for signal normalization), a common pseudo-reference gold electrode and a common gold counter-electrode. The electrode chips were connected to a potentiostat (Autolab PGSTAT128N, Metrohm; VSP, Bio-Logic) through an in-house-built connector box, and the nanocomposite coatings were electrochemically characterized in redox aqueous solution ($K_4Fe(CN)_6/K_3Fe(CN)_6$ 5 mM in 1 M KCl) by cyclic voltametry (scan rate 100 mV s^{-1} between −0.5 and 0.5 V versus open circuit potential) and EIS (0.1 MHz to 0.1 Hz, 5 mV amplitude versus open circuit potential, 50 measurements logarithmically spaced).

Characterization of nanocomposite coating by UV spectroscopy and circular dichroism. The composites were characterized by UV spectroscopy (Nanodrop 2000c, Thermo Scientific) before and after addition of GA to a final concentration of 1%, to elucidate changes in the absorbance bands of the peptide backbone or the aromatic rings due to the formation of the conjugated protein. Circular dichroism spectroscopy (J-815, Jasco) was used to characterize protein denaturation, formation of secondary structures due to conjugation with the nanomaterials[34,35] or protein loss due to centrifugation, sonication or cross-linking. The samples were diluted 1:25 in 10 mM potassium dibasic phosphate (Sigma-Aldrich, no. P3786) and 10 mM potassium monobasic phosphate (Sigma-Aldrich, no. P5655) buffer containing 140 mM sodium fluoride (Sigma-Aldrich, no. S7920), to reduce the high UV absorption of chloride ions in the lower region of the spectra.

Surface and topography characterization by SEM, TEM and AFM. Topographic characterization for the coatings was carried out by SEM (Ultra55, Zeiss), TEM (JEM-1400, JEOL) and AFM (Cypher, Asylum Research; DI-3100, Veeco). SEM characterization was carried out on nanocomposite coatings prepared on electrode chips. The samples were also coated with a thin layer of 5 nm Pt and Pd by sputtering (300T D, Quarum/EMS). Imaging was carried out by detection of secondary electrons using an in-lens detector at an accelerating voltage of 15 kV. For TEM characterization, Formvar/Carbon square grids (Electron Microscopy Sciences, no. FCF400-CU-SB) were first treated by glow discharge to render the carbon coating hydrophilic. Subsequently, a 1-μl sample of BSA, BSA/GA, AuNP, BSA/AuNP, AuNW, BSA/AuNW or BSA/AuNW/GA was deposited on the grid, wicked with a filter paper after 1 min and imaged at 80 kV. Nanocomposite coatings were prepared on freshly exposed mica substrates and characterized by AFM in non-contact tapping mode using tips with radius curvature <7 nm (Nanoandmore, no. PPP-FMR-10) to determine the morphology and roughness of the coating. Characterization of BSA and BSA/GA coating thickness was carried out by partially peeling off the substrate containing either coating.

Porosity calculation, pore density and average pore-to-pore distance. Analysis to determine the porosity of the BSA/AuNW/GA coating was carried out with ImageJ 1.52a (National Institutes of Health) on SEM images using the same protocol for all files. First, the image contrast background was increased at a specific threshold (up to 120, from 255 levels) where the pores were readily identified, then total pore number was counted considering circularity from 0 to 0.9. Porosity value (percentage of area occupied by pores) was extracted, as well as average pore radius (assuming the pores were perfect circles), and we also considered percentage of pores <20 nm as a relevant parameter (size of BSA). Pore density was calculated by dividing the number of pores by the area analysed. Pore-to-pore distance was calculated by considering the pores as being uniformly distributed across the area of the coating, then the average nearest-neighbour distance between the pores $\langle R_a \rangle$ could be calculated with the formula[36]:

$$\langle R_a \rangle = \frac{N_a^{-1/2}}{2} \quad (1)$$

where N_a is the number of particles per area.

The topographic data from AFM were analysed with Gwyddion 2.53 to extract the root mean square of the roughness, to measure the maximum pore depth and to calculate the average pore depth ($n = 100$).

Calculation of minimum pore-to-pore distance for steady-state behaviour considering diffusion of species. The minimum inter-micro-electrode distance required to avoid overlapping between adjacent diffusion layers can be estimated by the root mean square displacement of the electro-active diffusing particles using the following formula[37]:

$$\delta > 2\sqrt{2D\frac{\Delta E}{\nu}} \quad (2)$$

where D (cm^2 s^{-1}) is the diffusion constant of the reacting species, ΔE (V) is the potential difference between the onset of electrolysis and the potential at which steady-state current is obtained and ν (V s^{-1}) is the scan rate. Using the parameters $D = 7.4\times10^{-6}$ cm^2 s^{-1}, $\Delta E = 0.2$ V and $\nu = 1$ V s^{-1}, a minimum pore-to-pore distance for observation of steady-state currents should be $\delta > 34.4$ μm. Considering that the average pore-to-pore distance of our coating is only 59 nm, the electro-active species would diffuse rapidly and readily overlap neighbouring pores, yielding highly overlapped diffusion profiles.

Prediction of electrochemical behaviour of micro-electrode array/ensemble using Guo and Lindner theoretical framework. Guo and Lindner defined guidelines to design recessed microdisk electrode arrays, and constructed a

diagram based on different simulations to predict the behaviour of these arrays in cyclic voltammetry using dimensionless units[17]. We need to consider pore radius a (nm), pore-to-pore distance (in pore radius units) and the dimensionless scan rate V according to the formula:

$$V = \frac{nF\nu a^2}{4RTD} \quad (3)$$

where F (96,485 C mol^{-1}) is the Faraday constant, ν (V s^{-1}) is the scan rate, R is the gas constant, T (K) is the temperature and D (cm^2 s^{-1}) is the diffusion constant. Considering our average pore radius, $a = 19$ nm, the average nearest-neighbour distance between the pores, $d = 71$ nm ($3.7a$) and the fastest scan rate employed in our experiments, $\nu = 1$ V s^{-1} (4.8×10^{-6} dimensionless scan rate), we find that the predicted transient voltammogram (domain V)[17] is in good agreement with our results. We would have to reach scan rates of ~250 V s^{-1} or increase the average pore-to-pore distance from 71 to 228 nm to start observing quasi-steady-state behaviour (domain IV)[17]. Recessed electrodes obstruct the expansion of the diffusion layers, thereby delaying the overlapping of adjacent diffusion layers and effectively lowering the required pore-to-pore distance to achieve steady-state currents by up to 50%. However, even considering the recess, we would still expect highly overlapped diffusion layers.

In the case of BSA/AuNP coating (1:1,000 dilution), we consider $a = 10$ nm (AuNP radius) and the distance between the pores as $d = 193$ nm ($19.3a$), and therefore the distance between pores is sufficiently large and a quasi-steady-state behaviour is predicted (domain IV)[17].

Determination of diffusion-limited electrochemical processes with the Randles–Sevcik equation. Evaluation of voltammograms (peak current and peak-to-peak distance), at different scan rates, can be used to determine whether an analyte is freely diffusing in solution if the peak current i_p (A) of the oxidation and reduction is linearly correlated to the square root of the scan rate ν (V s^{-1}). This relationship is defined by the Randles–Sevcik equation[11]:

$$i_p = 0.446nFAC^0 \times \left(\frac{nF\nu D_0}{RT}\right)^{1/2} \quad (4)$$

where n is the number of electrons transferred in the redox event, A (cm^2) is the electrode geometric surface area, D_0 (cm^2 s^{-1}) is the diffusion coefficient of the analyte and C^0 (mol cm^{-3}) is the bulk concentration of the analyte.

Functionalization of BSA/AuNW/GA-coated electrodes with antibodies using carbodiimide chemistry. BSA/AuNW/GA-coated chips were functionalized with antibodies through carbodiimide activation of the carboxylic acid groups of the amino acids in BSA—that is, aspartic acid and glutamic acid. The chips were incubated with 400 mM *N*-ethyl-*N*′-(3-dimethylaminopropyl)carbodiimide (Sigma-Aldrich, no. 03449) and 200 mM *N*-hydroxysuccinimide (Sigma-Aldrich, no. 130672) in 0.1 M 2-(*N*-morpholino)ethanesulfonic acid buffer pH 6.0 (Sigma-Aldrich, no. M3671) for 30 min, rinsed with ultra-pure water and dried. Antibody solutions (20 µg ml^{-1}) were prepared in 0.5% glycerol in PBS and deposited on specific working electrodes using a ceramic hollowed needle (diameter 350 µm; LabNEXT, Inc., no. 007-350). Different combinations of antibodies could be spotted on different electrodes of the same chip to generate specific and control electrodes for different purposes and assays. The antibodies used were anti-PSA (Medix Biochemica, no. 100102), anti-IL-6 (Thermo Fisher Scientific, no. CHC1263), anti-insulin (R&D Systems, no. DY8056-05) and anti-glucagon (R&D Systems, no. DY1249). The chips were later incubated in a water-saturated atmosphere overnight at 4 °C, rinsed and washed with PBS in a shaker for 30 min. Then, 10 µl of 1-M ethanolamine (Sigma-Aldrich, no. E9508) in PBS, adjusted to pH 7.4 with HCl, was drop-cast on each electrode and incubated at room temperature for 30 min. Chips were thoroughly rinsed in ultra-pure water, dried and stored in 1% BSA at 4 °C for up to 1 month before use.

BSA/AuNW/GA coating optimization. The percentage of GA and concentration of BSA during preparation of the coating were optimized, with the latter ranging 0, 0.1, 1 and 5 mg ml^{-1} and the former ranging 0, 0.1, 1 and 5% (v/v). Coating time was optimized by 1-h, 4-h, 8-h, 1-d and 2-d incubation periods in BSA/AuNW/GA solution, after which the electrode chips were washed in PBS under shaking for 30 min. The coatings were characterized electrochemically before, and after, 1-d incubation in 1% BSA.

Calculation of linkage distribution of each BSA protein as a discrete probability distribution. Although the average binding site for a coating is, for instance, 3.9 as in the case of the coating 5 BSA/1 GA, we do not expect all BSA molecules to have exactly this number of bonds. With Poisson distribution[38] we can calculate the probability of observing each potential number of bonds between two BSA proteins according to the formula:

$$P(k \text{ events in interval}) = e^{-\lambda}\frac{\lambda^k}{k!} \quad (5)$$

where λ is the average linkage per BSA and k (%) is the number of linkages associated with BSA. So, for the coating 5 BSA/1 GA that has an average number of 3.9 pyridine polymer molecules—that is, linkages per BSA protein ($\lambda = 3.9$), we can calculate the percentage of BSA molecules with 0 linkages ($k = 0$) as 2.02%, BSA molecules with one linkage ($k = 1$) as 7.87%, two linkages as 15.36% and so on.

Antifouling properties and shelf-life of the coatings. The BSA/AuNW/GA-coated electrodes were challenged against 1% BSA, human serum and human plasma for 1 h, 1 d, 1 week and 1 month at 4 °C. Human plasma and serum samples were made from an anonymized apheresis collar, and aliquots were stored in propylene tubes at −80 °C. The results were compared against a bare gold electrode, and against gold electrodes coated with PEG-SAM, betaine-SAM or betaine/PEG-SAM. For the shelf-life storage test, BSA/AuNW/GA-coated electrodes were maintained under five different conditions: N_2 atmosphere at 4 °C, on the shelf at room temperature, PBS at room temperature, PBS containing 1% BSA and 0.05% Tween 20 at 4 °C and in a desiccator at 4 °C. After 1 month the electrodes were characterized by cyclic voltammetry.

Electrochemical enzymatic sandwich detection of IL-6 in human plasma. A laser-cut polymethyl methacrylate sheet, with inlet and outlet holes for liquid injection, was fixed on the surface of the electrode chips using a laser-cut, double-sided bonding tape channel to create an assay cell (internal volume 10 µl). All reagents and dilutions used in electrochemical enzymatic detection and the washing steps were prepared in assay buffer (1% BSA and 0.05% Tween 20 in PBS). The IL-6 biosensor chips were incubated with assay buffer for 30 min and flushed with 200 µl of assay buffer after each step. Soluble IL-6 (Thermo Fisher Scientific, no. CHC1263) was spiked at different concentrations in undiluted human plasma samples containing 1% (v/v) protease inhibition cocktail (Sigma-Aldrich, no. P8340) and incubated in the chips for 1 h. The biotinylated anti-IL-6 detection antibody (Thermo Fisher Scientific, no. CHC1263) was diluted to 1 µg ml^{-1} and incubated in the chips for 15 min. To complete the assay, poly-HRP streptavidin (Thermo Fisher Scientific, no. 21140) diluted 1:5,000 in assay buffer was incubated for 5 min. Precipitating TMB (Sigma-Aldrich, no. T9455) was incubated in the chips for 1 min. After the final flushing step, the electrodes were interrogated by cyclic voltammetry at a scan rate of 1 V s^{-1} between −0.5 and 0.5 V (versus open circuit potential). The electrodes were regenerated using 200 µl of 2-mM glycine hydrochloride (Sigma-Aldrich, no. G2879) and the assay was repeated immediately, then again after storage for 1 week and 1 month in 1% BSA at 4 °C.

Three other calibration curves were obtained under different conditions, using a different matrix (PBS and assay buffer) and/or a different coating (PEG-SAM). In these cases, all assay reagents including IL-6 were dissolved in PBS or assay buffer rather than human plasma, and performance was compared with a PEG-SAM-based antifouling coating.

Electrochemical impedance characterization of IL-6 biosensor fabrication and electrochemical enzymatic sandwich detection assay. Fabrication of the IL-6 biosensor and subsequent electrochemical enzymatic sandwich IL-6 detection assay were characterized after each step by EIS (Supplementary Fig. 8a). The R_{ct} of the working gold electrode surface at each assay step was determined by fitting the data from Nyquist plots (Supplementary Fig. 8b) to a Randles equivalent circuit (Supplementary Fig. 8c)[39]. The R_s models the resistance of the solution, the constant phase element (non-ideal capacitance) is used to model the double-layer capacitance (C_{dl}) and, in parallel, the R_{ct} and a Warburg element (Z_W) model the diffusion of electro-active species in solution. These fitting values, as well as the goodness of fitting (χ^2), for both IL-6-specific electrodes and insulin control electrodes, were extracted after each assay step and are presented in Supplementary Table 2.

BSA/AuNW/GA fouling test with PSA. All reagents were prepared in assay buffer (1% BSA and 0.05% Tween 20 in PBS at pH 7.0), and 200 µl was flushed into the chip after each step. BSA/AuNW/GA-coated electrodes functionalized with anti-PSA or anti-IL-6 antibodies, or non-functionalized, were incubated with 10, 0.1 or 0 ng ml^{-1} PSA (Biospacific, no. J63011) for 1 h. Detection antibody (1 µg ml^{-1}), labelled previously with HRP using a Lightning Link HRP Conjugation Kit (Expedeon, no. 701-0000), was incubated on the electrodes for 15 min. Precipitating TMB (Sigma-Aldrich, no. T9455) was incubated for 1 min and the electrodes interrogated by cyclic voltammetry at a scan rate of 1 V s^{-1} between −0.5 and 0.5 V (versus open circuit potential).

Calibration curve and LOD. The calibration curves for the different biosensors were built by measuring the current density of TMB oxidation at each concentration of IL-6 and fitting the values to a logarithmic relationship:

$$y = a \times \ln(x) + b \quad (6)$$

where y is the current density, x is the concentration of IL-6 and a and b are the fitting parameters. The nonlinear regression was fitted using the least-squares fitting method. LOD is defined as the concentration value of the calibration curve

(x_{LOD}) when y_{LOD} is the average current density of the blank plus threefold the s.d. of the blank:

$$\left(y_{LOD} = \overline{y_{blank}} + 3 \times \sigma_{blank}\right) \quad (7)$$

References

30. Gülseren, İ., Güzey, D., Bruce, B. D. & Weiss, J. Structural and functional changes in ultrasonicated bovine serum albumin solutions. *Ultrason. Sonochem.* **14**, 173–183 (2007).
31. Zhao, X., Lu, D., Hao, F. & Liu, R. Exploring the diameter and surface dependent conformational changes in carbon nanotube-protein corona and the related cytotoxicity. *J. Hazard. Mater.* **292**, 98–107 (2015).
32. Kopac, T., Bozgeyik, K. & Flahaut, E. Adsorption and interactions of the bovine serum albumin-double walled carbon nanotube system. *J. Mol. Liq.* **252**, 1–8 (2018).
33. Li, L., Lin, R., He, H., Jiang, L. & Gao, M. Interaction of carboxylated single-walled carbon nanotubes with bovine serum albumin. *Spectrochim. Acta A* **105**, 45–51 (2013).
34. Sekar, G., Pamela, S. B. E., Mukherjee, A. & Chandrasekaran, N. Spectroscopic studies of CNT induced fibrillar structures of BSA, haemoglobin and lysozyme. *Adv. Sci. Eng. Med.* **9**, 19–26 (2017).
35. Bhattacharya, M., Jain, N. & Mukhopadhyay, S. Insights into the mechanism of aggregation and fibril formation from bovine serum albumin. *J. Phys. Chem. B* **115**, 4195–4205 (2011).
36. Bansal, P. & Ardell, A. J. Average nearest-neighbor distances between uniformly distributed finite particles. *Metallography* **5**, 97–111 (1972).
37. Hwang, S. et al. CMOS microelectrode array for electrochemical lab-on-a-chip applications. *IEEE Sens. J.* **9**, 609–615 (2009).
38. Wang, X., Cohen, L., Wang, J. & Walt, D. R. Competitive immunoassays for the detection of small molecules using single molecule arrays. *J. Am. Chem. Soc.* **140**, 18132–18139 (2018).
39. Randviir, E. P. & Banks, C. E. Electrochemical impedance spectroscopy: an overview of bioanalytical applications. *Anal. Methods* **5**, 1098–1115 (2013).

Acknowledgements

This research was supported by funding from the Wyss Institute for Biologically Inspired Engineering (to D.E.I.), Defense Advanced Research Projects Agency under Cooperative Agreement (no. W911NF-12-2-0036, to D.E.I.), the Institute for Basic Science (no. IBS-R020-D1) and by a gift from the KeepSmilin4Abbie Foundation. This work was performed in part at the Center for Nanoscale Systems of Harvard University, a member of the National Nanotechnology Coordinated Infrastructure Network, which is supported by the National Science Foundation under NSF award no. 1541959.

Author contributions

Conception and experimental design were performed by J.S.R., P.J., O.Y.F.H. and D.E.I. Experiments were carried out by J.S.R. and P.J. Validation and reproducibility were performed by P.J and O.Y.F.H. Data analysis was carried out by J.S.R., P.J., O.Y.F.H. and D.E.I. All authors discussed the results and contributed to writing the manuscript.

Competing interests

The authors are listed as inventors on patents describing this technology.

Additional information

Supplementary information is available for this paper at https://doi.org/10.1038/s41565-019-0566-z.

Correspondence and requests for materials should be addressed to D.E.I.

Reprints and permissions information is available at www.nature.com/reprints.

nature research

Corresponding author(s): Donald Elliot Ingber

Last updated by author(s): Sep 24, 2019

Reporting Summary

Nature Research wishes to improve the reproducibility of the work that we publish. This form provides structure for consistency and transparency in reporting. For further information on Nature Research policies, see Authors & Referees and the Editorial Policy Checklist.

Statistics

For all statistical analyses, confirm that the following items are present in the figure legend, table legend, main text, or Methods section.

n/a	Confirmed	
☐	☒	The exact sample size (*n*) for each experimental group/condition, given as a discrete number and unit of measurement
☐	☒	A statement on whether measurements were taken from distinct samples or whether the same sample was measured repeatedly
☐	☒	The statistical test(s) used AND whether they are one- or two-sided *Only common tests should be described solely by name; describe more complex techniques in the Methods section.*
☐	☒	A description of all covariates tested
☐	☒	A description of any assumptions or corrections, such as tests of normality and adjustment for multiple comparisons
☐	☒	A full description of the statistical parameters including central tendency (e.g. means) or other basic estimates (e.g. regression coefficient) AND variation (e.g. standard deviation) or associated estimates of uncertainty (e.g. confidence intervals)
☐	☒	For null hypothesis testing, the test statistic (e.g. *F*, *t*, *r*) with confidence intervals, effect sizes, degrees of freedom and *P* value noted *Give P values as exact values whenever suitable.*
☒	☐	For Bayesian analysis, information on the choice of priors and Markov chain Monte Carlo settings
☒	☐	For hierarchical and complex designs, identification of the appropriate level for tests and full reporting of outcomes
☒	☐	Estimates of effect sizes (e.g. Cohen's *d*, Pearson's *r*), indicating how they were calculated

Our web collection on statistics for biologists contains articles on many of the points above.

Software and code

Policy information about availability of computer code

Data collection	Electrochemical data was acquired using Nova 1.11 and EC-Lab(R) Software V11.20. AFM topography was acquired with Asylum AR14 (Igor 6.3) and Nanoscope (R) IIIa 5.31R1. TEM images were acquired with TEM Center 1.3.4.2698. SEM imaged were acquired with SmartSEM 5.09. Circular dichroism spectra was acquired with Spectrum Manager 2 UV spectra was acquired with NanoDrop 1.6.198
Data analysis	Data analysis was carried out using Office Excel 2019, Prism 7, ImageJ 1.52a and Gwyddion 2.52

For manuscripts utilizing custom algorithms or software that are central to the research but not yet described in published literature, software must be made available to editors/reviewers. We strongly encourage code deposition in a community repository (e.g. GitHub). See the Nature Research guidelines for submitting code & software for further information.

Data

Policy information about availability of data

All manuscripts must include a data availability statement. This statement should provide the following information, where applicable:

- Accession codes, unique identifiers, or web links for publicly available datasets
- A list of figures that have associated raw data
- A description of any restrictions on data availability

The data that support the plots within this paper and other findings of this study are available from the authors upon reasonable request.

Field-specific reporting

Please select the one below that is the best fit for your research. If you are not sure, read the appropriate sections before making your selection.

☒ Life sciences ☐ Behavioural & social sciences ☐ Ecological, evolutionary & environmental sciences

For a reference copy of the document with all sections, see nature.com/documents/nr-reporting-summary-flat.pdf

Life sciences study design

All studies must disclose on these points even when the disclosure is negative.

Sample size	We carried out quadruplicates for each condition tested in order to, at least, have a triplicate in case we lose one due to human error. A triplicate already offers precision in the measurements to have confidence in average measured values and to determine a standard deviation. Also, our findings were validated by three investigators and have been continuously used ever since.
Data exclusions	The exclusion criteria during data acquisition was pre-established based upon the unwanted external interference with the experiment. For instance, electrochemical data could be excluded if voltammograms or impedance spectra showed only noise, clearly indicating that the electrodes or electric paths were defective (cut) or connections were not properly connected. Electrochemical data could also be eliminated during acquisition due to human mistake, for instance starting the experiment in wrong conditions, or due to accidents during acquisition (touching electrodes during measurement or spilling the solution). All these issues were always confirmed (for instance checking under the microscope that the electric path of the electrode was cut and that was the reason for the noise) before repeating the experiment, and no data was excluded during analysis.
Replication	The findings described in the manuscript reporting the fabrication of the optimum antifouling coating were validated by three investigators (the first three authors of the manuscript). They followed the protocols described to obtain an antifouling coating on the electrode chips using triplicates, they measured the electrochemical properties (current density and peak-to-peak separation) right after the coating was prepared and after 1-day incubation in 1% BSA and confirmed that the electrode were as good as expected. Moreover, this protocol has been used continuously by author 1 and 3 in different laboratories to fabricate electrochemical affinity biosensors for measuring biomarkers present in complex media ever since.
Randomization	Randomization was not relevant in our studies because there was no possibility of selection bias, i.e. we did not have to select samples/chips from a pool. All the chips used for replication were identically the same, and the selection of parameters like the nanomaterial used in the composition of the coating, concentration of BSA or GA and incubation time, were properly tested in specific fouling assays or selected through optimization assays using a range of conditions.
Blinding	Blinding was not relevant in our studies because we did not have a preference for the materials or the conditions used.

Reporting for specific materials, systems and methods

We require information from authors about some types of materials, experimental systems and methods used in many studies. Here, indicate whether each material, system or method listed is relevant to your study. If you are not sure if a list item applies to your research, read the appropriate section before selecting a response.

Materials & experimental systems

n/a	Involved in the study
☐	☒ Antibodies
☒	☐ Eukaryotic cell lines
☒	☐ Palaeontology
☒	☐ Animals and other organisms
☒	☐ Human research participants
☒	☐ Clinical data

Methods

n/a	Involved in the study
☒	☐ ChIP-seq
☒	☐ Flow cytometry
☒	☐ MRI-based neuroimaging

Antibodies

Antibodies used	- Human anti-PSA (capture)(Product #100102, Lot #0038604, Medix Biochemica, USA). Clone number not provided. 20 µg/mL - Human anti-PSA (detection) (Product #100103, Lot #0037434, Medix Biochemica, USA). Clone number not provided. 1 µg/ml - IL6 Human Matched Antibody Pair (capture) (Product #CHC1263, Lot #170401, Thermo Fisher Scientific, USA). Clone number not provided. 20 µg/mL - IL6 Human Matched Antibody Pair (biotinylated) (Product #CHC1263, Lot #170401, Thermo Fisher Scientific, USA). Clone number not provided. 1 µg/ml - Human anti-insulin (capture) (Product #DY8056-05, Lot# P124761, R&D Systems, USA). Clone number not provided. 20 µg/mL - Human anti-insulin (biotinylated) (Product #DY8056-05, Lot# P124761, R&D Systems, USA). Clone number not provided. 1 µg/ml

- anti-glucagon (capture) (Product #DY1249, Lot #CCMM0414121, R&D Systems, USA). Clone number not provided. 20 µg/mL
- anti-glucagon (biotinylated) (Product #DY1249, Lot #HVE0114121, R&D Systems, USA). Clone number not provided. 1 µg/ml

Validation

- anti-PSA set: Immunoreactivity of 80–120 % compared to the reference sample in an FIA test (https://www.medixbiochemica.com/en/antibodies-antigens/tumor-markers/#anti-h-psa-8301-sprn-5)
- anti-IL6 set: A calibration curve is provided in the website as well as a list of 17 publications citing the use of the set. (https://www.thermofisher.com/elisa/product/IL-6-Human-Matched-Antibody-Pair/CHC1263)
- anti-insulin: A calibration curve is provided in the website as well as 1 publications citing the use of the set (https://www.rndsystems.com/products/human-canine-porcine-insulin-duoset-elisa_dy8056-05#product-citations)
- anti-glucagon: A calibration curve is provided in the website as well as 2 publications citing the use of the set (https://www.rndsystems.com/products/glucagon-duoset-elisa_dy1249)